Substrate-Free Self-Assembly Approach toward Large-Area Nanomembranes

Fei Wang,[†,‡] Jung-Hun Seo,[§] Zhenqiang Ma,[§] and Xudong Wang[†,*]

[†]Department of Materials Science and Engineering, [‡]Department of Chemistry, and [§]Department of Electric and Computer Engineering, University of Wisconsin—Madison, Madison, Wisconsin 53706, United States

I n the frontier of nanoscience and nano-technologies, there has been an ever-growing interest in novel free-standing two-dimensional (2D) nanostructures owing to their intriguing application potentials for flexible thin-film transistors, optoelectronics, sensors, actuators, energy harvesting, and storage devices.[1−3] Among them, the most representative materials are graphenes[4,5] and semiconductor nanomembranes (NMs).[6,7] In comparison to one-dimensional (1D) nanostructures that face daunting engineering challenges in large-scale integration, 2D geometry is compatible with the existing fabrication and assembly technologies stemming from decades of research and scrutiny in microelectronic industry. Their free-standing feature allows them to be transferred onto arbitrary substrates, including flexible substrates, which in many cases are incompatible with most high-temperature epitaxial growth techniques.[8,9] Therefore, they hold great promises for applications in which conventional wafer-based technologies fail to address the requirements, such as flexible transparent electronics and conformal medical devices.[10] To date, high-frequency transistors,[11] photo-detectors,[12] light-emitting diodes,[13] and biomedical sensors[14,15] have been demonstrated using NMs made from silicon,[16] gallium arsenide (GaAs),[14] and gallium nitride (GaN).[17] Nevertheless, broader applications desire NMs from more functional materials with low-cost and less sophisticated fabrication approaches.

The prominent methods of producing semiconductor NMs involve the use of specialized anisotropic etching or chemically selective etching of sacrificial layers. For example, the creation of silicon NMs relies on defining trenches on (111)-oriented Si wafers and selective removal of materials along the [110] direction[18] or the selective etching of silicon dioxide in silicon-on-oxide (SOI) wafers.[19] GaAs NMs are fabricated by

ABSTRACT
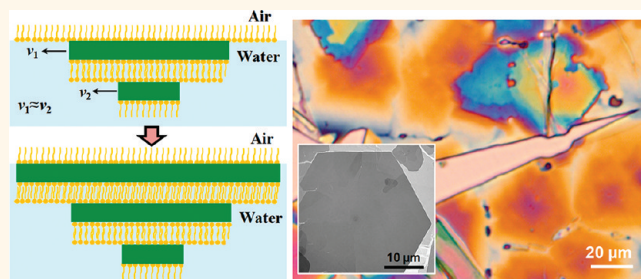
Free-standing two-dimensional nanostrucutures, such as graphene and semiconductor nanomembranes (NMs) featuring their integration with flexible polymer substrates, address applications in which electronic devices need to be stretchable or conformally positioned to nonplanar surfaces. We report a surfactant-directed surface assembly approach to producing large-area NMs at the water−air interface. The NMs were produced by employing the surfactants as templates as well as incorporating them in the crystal structures. By using excess amount of sodium dodecylsulfate (SDS), a tightly packed monolayer of dodecylsulfate (DS) ion was formed and directed the crystallization of submillimeter-sized zinc hydroxy dodecylsulfate (ZHDS) single-crystalline NMs over the entire water surface. This free-standing NM can be readily transferred to an arbitrary substrate and converted to ZnO *via* heat treatment. A flexible thin-film transistor was also fabricated using the transferred NMs and demonstrated reasonably good n-type transport properties. This approach circumvented the needs of single-crystalline substrates for making large-area NMs from materials that do not possess a laminate structure. It is a low-cost and large-scale synthesis technique and has great potential in developing NMs and flexible devices from various functional materials that are not feasible by conventional selective etching or delamination approaches.

KEYWORDS: two-dimensional nanostructure · free-standing · nanomembranes · surfactant monolayer

etching off sacrificial aluminum gallium arsenide from multilayer expitaxial films.[20] In general, the sacrificial layer should have distinguishing chemical properties to allow selective etching. Meanwhile, its crystal structure should be nearly identical to the NM material so that high-quality single-crystalline NMs can be grown epitaxially. Therefore, the choices of NM materials are largely limited by the availability of sacrificial layers. As is done for graphene, exfoliation
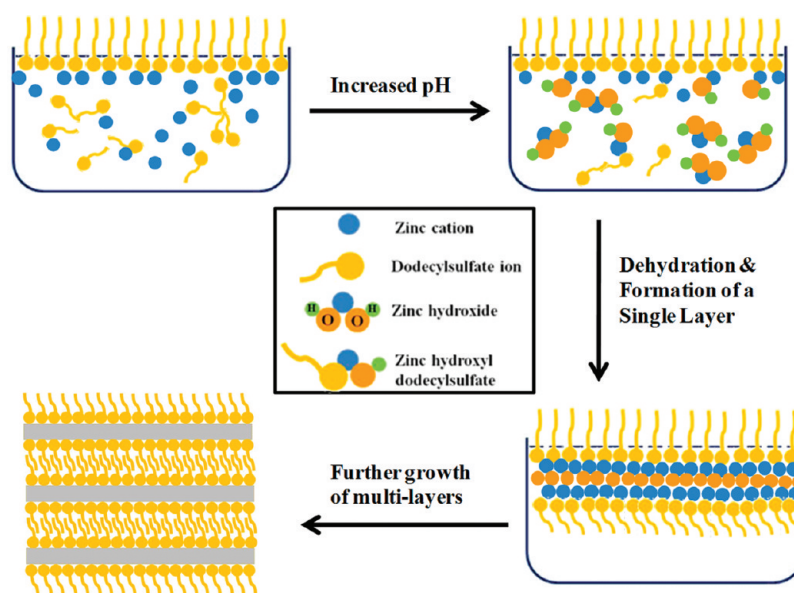
Figure 1. Schematic illustration of the formation process of ZHDS NMs at the water surface assisted by DS ions.

of naturally layered materials such as MoS_2 offers another route to 2D nanostructures.[21,22] However, the availability of layered semiconductors has always been a constraint of considering exfoliation as a general method for producing NMs. The recent success in solution synthesis of lead sulfide by oriented attachment[23] and ceria ultrathin nanosheets by controlled precursor supply[24] showed good promises in producing large quantities of 2D nanostructures, but their sizes remained in the submicrometer regime.

Surfactants are commonly used in nanomaterials syntheses to modify the morphology of inorganic crystals. In addition to microemulsion synthesis, the mechanisms are generally perceived to be the selective adsorption of surfactants onto certain crystallographic facets. Alternatively, the other important behavior of surfactants (*i.e.*, the close-packed monolayer [Langmuir–Blodgett (LB) film] at the water–air interface) can also be applied to directing crystal growth. Emulating biomineralization, epitaxial growth under LB films has been used to synthesize facet-controlled inorganic crystals. For example, using a LB film composed of arachidic acid (AA), PbS, CdS, and PbSe nanocrystals were epitaxially grown at the liquid–air interface *via* reactions between soluble metal precursors and reactive gases.[25,26] Metal nanoparticle films, such as Ag, have also been synthesized from $AgNO_3$ and formaldehyde under a LB film of dihexadecyl phosphate.[27] Inspired by this strategy, we developed a surfactant-directed surface assembly approach to producing large-area NMs at the water–air interface. The NMs were produced by employing a monolayer of the dodecylsulfate (DS) ions as templates, as well as incorporating them in the crystal structures. Free-standing NMs composed of submillimeter-sized single-crystalline zinc hydroxy dodecylsulfate (ZHDS) were formed over the entire water surface. They can be transferred to an arbitrary substrate and converted to ZnO *via* heat treatment. A flexible thin-film transistor was also demonstrated using the transferred NMs. This approach circumvented the needs of single-crystalline substrates for making large-area NMs from materials that do not possess a laminate structure.

Synthesis Strategy. Figure 1 illustrates the formation strategy of ZHDS NMs on the water surface. Zinc nitrate and hexamethylenetetramine (HMT) are two well-known precursors to produce zinc oxide nanostructures in aqueous solutions.[28] However, in the presence of sulfate ions, both the composition and the morphology of the products are dramatically changed. Elemental zinc and zinc ions often mineralize to zinc hydroxy sulfate hydrate in the presence of sulfate ions.[29] Morin *et al.* recently reported the formation of zinc hydroxy sulfates semihydrate ($3Zn(OH)_2 \cdot ZnSO_4 \cdot 0.5H_2O$) (ZHS) microplates when $ZnSO_4$ was added to the ZnO growth system.[30] In fact, the erosion of zinc metal in the presence of sulfate ions or chloride ions has been known to produce similar compounds, although the degree of hydration and the ratio between hydroxides and sulfates may vary.[31] Therefore, it would not be surprising that DS ions, containing sulfate groups, could alter the composition of the products from the two precursors that normally would produce 1D ZnO and convert the morphology to 2D. There have been a number of reports on the synthesis of $Zn(OH)_2$/DS layered composite films, including electrodeposition[32,33] and chemical reaction between zinc nitrate and HMT.[34,35] Different from those reported, we used an excess amount of sodium dodecylsulfate (SDS) surfactants above the critical micelle concentration (CMC) to form a densely packed DS ion monolayer on the water surface. As depicted in Figure 1, DS ions form a negatively
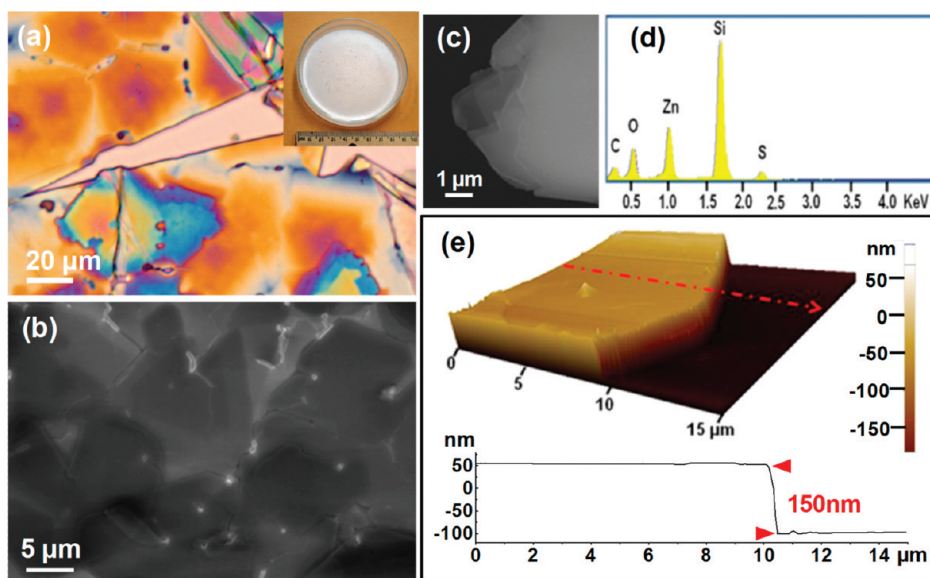
Figure 2. Structural characterization of ZHDS NM. (a) Optical microscopy image of a ZHDS NM supported by a Si substrate. The inset is a photo of the as-synthesized NM on the water surface in a glass dish. **(b)** SEM image of ZHDS NMs on a Si substrate. **(c)** SEM image taken at the edge of a ZHDS NM showing the layered structure. **(d)** EDX spectrum of ZHDS NMs showing the elementary composition. **(e)** AFM topological image of a single hexagonal ZHDS grain showing the flat surface and a thickness of ∼150 nm.

charged monolayer at the wafer surface, under which zinc cations are enriched and an electrostatic double layer is formed. As the temperature increases, the pH value of the solution, buffered by HMT and its thermal decomposition to ammonia, also increases, which initiates the crystallization of ZHDS both underneath the DS ion monolayer and in the bulk solution. Because there is also a significant amount of DS ions in the bulk solution, zinc ions are also in the form of $ZnDS_2$ and ZHDS, in addition to all forms of zinc hydroxyl species $(Zn(OH)_m{}^{m-2}, m = 0$ to 4). Zinc hydroxyl species, as well as $Zn(OH)_xDS_y$ species, diffuse to the water surface and participate in the crystallization of ZHDS on the water surface. The DS ions stay in the crystal in a tail-to-tail configuration with sulfate heads bonding with zinc ions. This creates a layered structure with alternating zinc hydroxide layers and double hydrophobic DS tail layers.

Morphology and Structure Analyses. Because of the continuous distribution of the DS ion monolayer, the as-synthesized ZHDS NM can completely cover the entire water surface in the container, as shown in the inset of Figure 2a. The size of the continuous ZHDS NM is only limited by the opening area of the reaction vessel. The photo was taken at an angle, from which the contrast of the NM is maximized so that the NM is distinguishable. Transferring of the NM to a substrate was done by inserting the substrate below the floating NM and slowly scooping up. The NMs exhibited good flexibility and integrity and can cover the entire substrate surface while remaining intact (Figure S1 in Supporting Information). Figure 2a shows such a NM that was transferred onto a silicon substrate. The color contrast is

the consequence of optical interference that results from nonuniformity in thickness. From red to blue, the thickness decreases. Some radical patterns of color gradient in this image imply the existence of surface pyramids, which will be discussed later in detail. The color contrast also suggests the approximate grain size, which is from ∼50 to >100 μm. The cracks and wrinkles were formed during NM transfer from the water surface to the substrate and/or during the drying of water. Figure 2b is a scanning electron microscopy (SEM) image of a NM with smaller grain size supported on a silicon substrate. It clearly reveals that the NM is actually composed of hexagonal-like plates. These plates overlap to the extent that the overall NM is continuous. Very small open spaces can still be observed at the boundary where the plates meet. At the exposed edge, the layered structure can be visualized possibly due to the nonuniform lateral growth of each layer (Figure 2c). The elemental composition of the NM is confirmed by the energy-dispersive X-ray spectroscopy (EDS) equipped in the SEM chamber (Figure 2d). Signals from Zn, O, C, and S can all be clearly detected, supporting the possibility of the ZHDS component. The topography of a single grain was analyzed by atomic force microscopy (AFM), as shown in Figure 2e. A fairly flat top surface was demonstrated with a surface roughness of ±2 nm. The thickness was determined to be ∼150 nm for the NM that was grown for 4 h.

The layered structure of the ZHDS NM was confirmed by small-angle X-ray diffraction (XRD), as shown in Figure 3a. The intensity of the reflection peaks decreases as the order of the peaks increases. From the position of the first peak (2.2°), the periodicity of
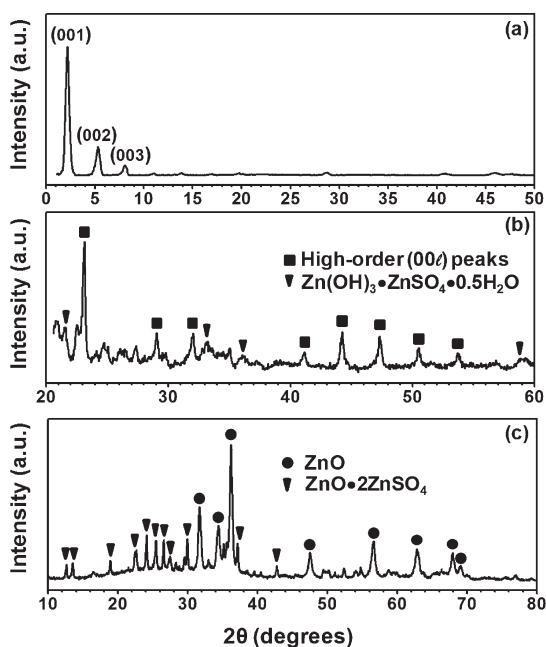
Figure 3. (a) Small-angle X-ray diffraction of as-synthesized ZHDS NMs. (b) Wide-angle X-ray powder diffraction of ZHDS NMs. (c) Wide-angle X-ray powder diffraction of ZHDS NMs annealed at 500 °C for 12 h.
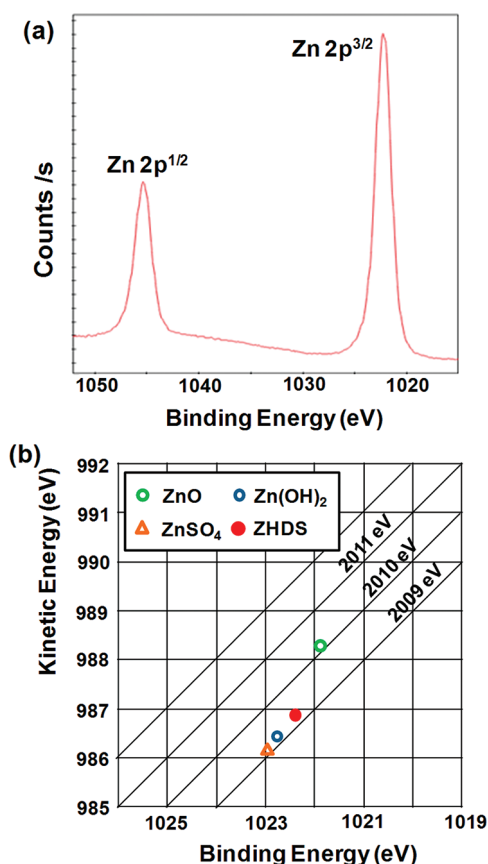

Figure 4. XPS analysis of as-synthesized ZHDS NMs. (a) XPS spectra showing Zn 2P peaks; (b) Wagner plot showing the modified Auger parameter of Zn in ZHDS as well as Zn in ZnO, $ZnSO_4$, and $Zn(OH)_2$, retrieved from NIST XPS database.

the layered structure is estimated to be 4.0 nm, which consists of an inorganic ZH layer and a double layer of DS ions. To further identify the crystallographic structure of ZHDS NM, powder diffraction patterns were also collected, where the high-order reflection peaks resulting from the layered structure also appeared (Figure 3b). The crystal structure of ZHDS could be viewed as a derivative of that of ZHS, in which octahedral coordinated zinc cations have a six-fold symmetry in the zinc hydroxyl layer while divalent sulfate ion (as well as water molecules in the hydrated form of ZHS) layers bridge the zinc hydroxyl layers.[36] In the ZHDS crystal structure, DS ions substitute sulfate ions in ZHS crystals. The hydrocarbon tails of DS ions overlap by hydrophobic interactions and form an effectively Gemini surfactant layer, bridging the zinc hydroxyl layers and leaving them unchanged.[37,38] In Figure 3b, four peaks can be indexed to $3Zn(OH)_2 \cdot ZnSO_4 \cdot 0.5H_2O$ (ZHS) (PDF no. 44-0674) (110), (120), (030), and ($1\bar{5}0$) planes. These are all (hk0) planes, which supports that the crystal structure of the ZHDS NMs is a derivative from ZHS hydrate, as the zinc hydroxyl layers in ZHDS should have the same lattice parameters as those in ZHS while the c value is significantly augmented by the intercalation of the hydrocarbon tails of DS ions. The sample was then annealed in air at 500 °C for 12 h to burn off the organics and dehydrate zinc hydroxide. Corresponding XRD pattern is shown in Figure 3c. After annealing, all XRD peaks can be indexed to two phases: zinc oxide sulfate ($ZnO \cdot 2ZnSO_4$, PDF no. 32-1476) and wurtzite ZnO (PDF no. 36-0451). This result suggests that the hydrocarbon tails and hydroxyl groups can be

completely removed at elevated temperature, whereas the sulfate groups still exist in the form of zinc oxide sulfate. How to effectively remove the sulfate groups from the NMs would be a critical challenge to receive pure ZnO phase.

In order to further confirm the chemical environment of zinc, X-ray photoelectron spectroscopy (XPS) was used to characterize the ZHDS NM on the Si substrate. The Zn 2p 1/2 and Zn 2p 3/2 peaks appear at 1045 and 1022 eV, respectively (Figure 4a). To interpret the chemical environment of zinc from XPS results, modified auger parameter (α', the sum of kinetic energy of the Auger transition and Zn 2p 3/2 binding energy) of the as-grown ZHDS NM was plotted in the Wagner plot (chemical state plot), as shown in Figure 4b. The Auger kinetic energy is on the ordinate, and the photoelectron binding energy is on the abscissa oriented in the negative direction. To a good approximation, the shifts in the modified auger parameter (shown in the diagonal line) between two chemical states are different in the extra-atomic relaxation (ΔR^{ea}) or the polarization energy arising from the neighboring ligands.[39] Standard modified Auger parameters of $Zn(OH)_2$, $ZnSO_4$, and ZnO were retrieved from the NIST XPS database. Figure 4b shows that the modified
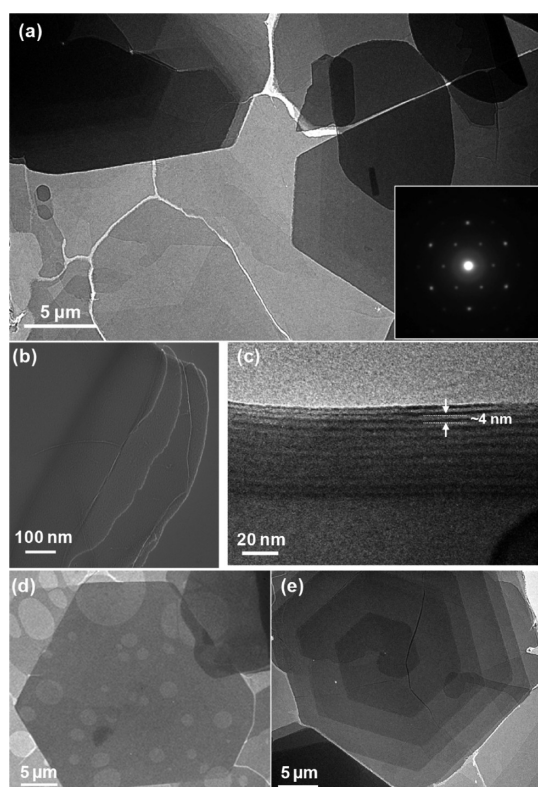
Figure 5. TEM characterization of ZHDS NMs. (a) Large-area TEM image where multiple grains can be seen. Inset is the electron diffraction pattern of a single NM grain, where the six-fold symmetry can be clearly seen. (b) Edge of a single NM grain showing the multilayer structure. (c) High-magnification TEM image of a curled edge where the multilayer structure can be observed. The periodicity is measured to be ~4 nm. (d) Hexagonal single grain with flat surface. (e) Hexagonal single grain with obvious surface hillocks.

Auger parameter of the ZHDS NM lies in line with those of $Zn(OH)_2$ and $ZnSO_4$, but not ZnO. This is in agreement with the discussed bonding situation: zinc cations are coordinated by hydroxides and sulfates.

The morphology and crystal structure of the ZHDS NMs were further characterized by transmission electron microscopy (TEM). It is worth mentioning that the ZHDS NMs deteriorated very quickly under the illumination of focused electron beam, which is a direct result of the charging effect by the nonconductive DS ion layers. Figure 5a was snapped at a low magnification and further revealed that the ZHDS NMs comprised individual overlapping hexagonal grains. By taking the electron diffraction pattern at each individual grain, we found that each of them was a single crystal (inset of Figure 5a). However, when including multiple grains in the beam spot, we observed multiple sets of hexagonal single-crystalline diffraction patterns with angle offsets, suggesting the misalignment between each grain and the others in the vicinity. Figure 5b shows the edge of a single-crystal NM where the layers are not perfectly overlapping and thus observable. The curled edge of another single-crystal NM in Figure 5c also reveals the layered structure in ZHDS.

The curled edge reveals the cross section of one NM grain, where the dark stripes and bright stripes correspond to the alternating inorganic and double DS layers, respectively. The layer thickness was measured to be ~4.0 nm, which is in good agreement with XRD data (see Figure 3a). Two typical morphologies of individual single-crystalline grains are shown in Figure 5d,e, respectively, where one has fairly uniform contrast (Figure 5d) and the other one showed obvious helical contours (Figure 5e). The grain with helical contours is the dominating morphology in observed NMs. Affirmatively, the contrast comes from thickness of the NM, and the helical contours thus represent morphologically hillock-like pyramids. This is indicated in Figure 1a and unveiled by SEM and AFM analyses, respectively. AFM topographic scan revealed a grain from ZHDS NMs with hillock step heights of ~8 nm multiples (Figure S2).
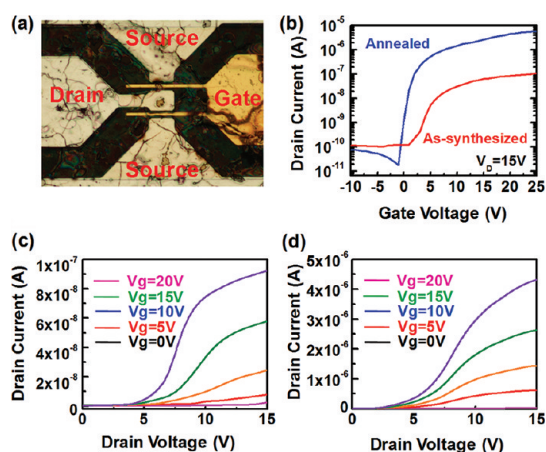
Formation Mechanism. Similar surface hillocks have also been observed on ZHS plates and were proposed to be a result of screw dislocations.[29,40] We believe that the growth of ZHDS NMs was also driven by screw dislocations because of the similar crystal structures and surface hillock features. In order to further verify this mechanism, the morphology of ZHDS NMs at different growth time points was investigated by TEM (Figure S3). After a 15 min reaction, hexagonal plates smaller than 2 μm were observed. Majority of these plates exhibited a pore in the center. This is a common phenomenon due to strain relaxation associated with screw dislocations, known as dislocation pipes, which is often seen in screw-dislocation-rich materials such as GaN.[41,42] As the growth proceeded, the size of the hexagonal plates continuously increased and eventually reached ~10 μm in diameter after 90 min (Figure S2b−d). The dislocation pipes were also closed during the growth because crystal growth in the dislocation pipes is energetically easier.[43] The size of single-crystalline grains could reach >100 μm given longer growth time.

Evolution of the flat and wide hillock steps from screw dislocations was suggested to be the result of the comparable lateral growth rates of all hillock step edges, where the growth of the hillock steps formed later cannot catch up with earlier formed ones. This would also be the key feature that led to the formation of continuous NMs covering the entire water surface. In order to illustrate this mechanism, we denote the growth rates of the first NM layer and the rest layers as v_1 and v_2, respectively, as shown in Figure 6. Because of surfactant tails exposed on top of the ZHDS layers, the ledges at the ZHDS growth front are favorable deposition sites due to hydrophobic interaction between the hydrocarbon tails. Thus, fast v_2 could always be obtained. When a surfactant monolayer appears on the water surface, it provides a similar deposition ledge as those of the rest of the layers directing the growth of
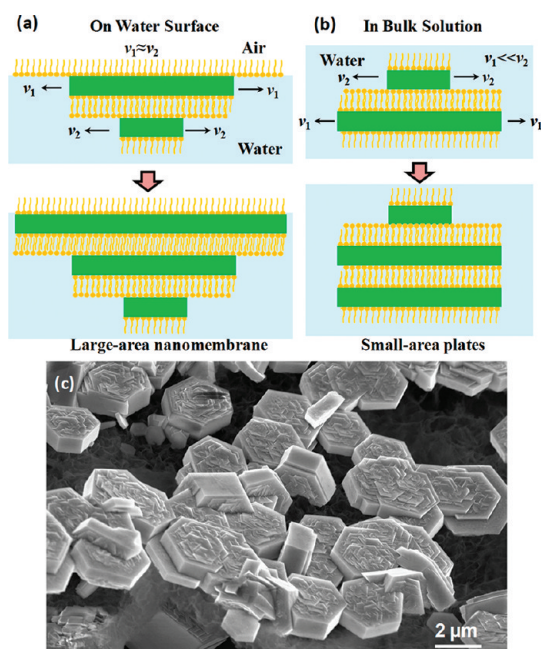
Figure 6. Schematic drawing that illustrates the difference in the evolution of the hillock steps between the large-area NMs grown on the water surface (a) and small-area plates precipitated from the bulk solution (b). In case (a), the DS ion monolayer at the water surface leads to comparable v_1 and v_2 and large NM is formed. In the absence of the DS ion monolayer, v_1 is significantly limited, so small and thick plates are produced. (c) ZHDS micrometer-sized plates grown inside bulk solution. The hillock steps are obvious on the surface of the plates.

Figure 7. (a) Optical microscope image showing a ZHDS NM-based FETs on a PET substrate. Channel length and width are 20 and 5 μm, respectively. (b) Transfer characteristics of FETs before (red) and after (blue) annealing at 95 °C for 48 h. (c,d) Output characteristics of as-synthesized (c) and annealed (d) samples measured from $V_D = 0-15$ V and $V_G = 0-20$ V with 5 V steps.

the first layer of NM, resulting in comparable v_1 and v_2. Therefore, large-area NM can be formed without significant thickening of the ledges, and clear hillocks are always shown (Figure 6a). This mechanism is further proved by the products obtained from bulk solution, where no large surfactant layer is presented. Without the assistant of the surfactant layer, v_1 is significantly suppressed, while v_2 is unaffected. Therefore, $v_2 \gg v_1$, and thereby the later formed growth ledge can quickly catch up with the earlier formed layers, leading to the formation of small and thick disks in bulk solution (Figure 6b). The corresponding products are shown in Figure 6c, where the hillocks on the surface can still be clearly observed. The different morphology of ZHDS on the water surface and in the bulk solution supports the importance of the surface DS ion monolayer in directing the growth of large-area NMs. This growth mechanism suggests that the formation of NMs should be dictated by the reactions at the water surface. Although micelles with various morphologies can be formed at different concentrations and temperature regimes when the surfactant concentration is above its CMC, the micelles do not have a direct relationship with the NM growth at the water/air interface. As evidenced by TEM analysis, the DS ion double layers are part of the crystal structure of ZHDS and are unlikely to be a result of the existence of micelles in the bulk solution.

Electrical Properties. The large-area substrate-free NM offers great advantages in fabricating flexible electronic devices. Field-effect transistors (FETs) were fabricated by transferring the free-standing ZHDS NM onto a plastic substrate. Standard photolithography, dielectric and metal evaporation, and liftoff processes were used to form source/drain contacts with Ti/Au, gate dielectric, and the contact between SiO$_x$ and Ti/Au. Details of the device fabrication procedure are illustrated in Figure S4. ZHDS FETs with a channel width of 20 μm and a length of 5 μm are shown in Figure 7a. The electrical transport characteristics shown in Figure 7b clearly demonstrated an n-type behavior. Drain current was significantly improved by annealing the device at 95 °C for 48 h in a convection oven after device fabrication. The detail electrical characteristics, that is, the saturation mobility (μ_{sat}) and the threshold voltage (V_{TH}), were calculated and extracted by eq 1

$$I_{DS} = \frac{1}{2}\left(\frac{WC_{OX}\mu_{sat}}{L}\right)(V_{GS} - V_{TH})^2 \quad (1)$$

where W and L are channel width and length, C_{ox} is the capacitance per unit area of dielectric layer, and μ_{sat} is the saturation mobility. After the heat treatment, μ_{sat} was increased from 0.0027 to 0.12 cm^2/V·s for $V_{DS} = 15$ V, and corresponding on/off ratio was improved from 10^3 to 3×10^5. V_{TH} calculated by fitting a slope to the plot of the square root of drain current *versus* gate bias was decreased from 1 to 0.6 V. These improvements could be attributed to the removal of water from the layered structure and/or dehydration of the hydroxyl groups. Figure 7c,d shows the output characteristics of as-synthesized and annealed ZHDS-NM FETs measured from $V_D = 0-15$ V and $V_G = 0-25$ V with 5 V steps, respectively. In both cases, the degree of saturation of drain current is similar, while the drain current

was efficiently suppressed at a low gate bias region from the annealed device, which is advantageous in terms of power saving at an off state.

CONCLUSION

In this paper, we reported a novel strategy of synthesizing large-area free-standing crystalline NMs without using any crystalline substrates. The formation of NMs was directed and templated by self-assembled surfactants in a form of monolayer on the water surface as well as incorporated inside the crystal. The experiments used excess SDS as surfactants in a conventional solution for making ZnO nanostructures. Due to the incorporation and self-assembly of DS ions, continuous ZHDS NMs were formed covering the entire water surface. The NM was composed of overlapping single-crystalline hexagonal ZHDS plates with the size ranging from ∼10 to >100 μm. It is possible to grow single-crystalline plates with even larger size by engineering the molecular structure of the surfactant and controlling the surface pressure by a LB film apparatus to improve the alignment of the surfactants in the surface monolayer. Heat treatment can effectively remove the hydrocarbon component and dehydrate the hydroxyl groups, and thereby converts ZHDS into ZnO. However, removing the sulfate group appeared to be a challenge for reaching the pure ZnO phase. The ZHDS NM also demonstrated a good potential for making flexible electronic devices. This approach is a low-cost and large-scale synthesis technique and is promising for developing NMs and flexible devices from various functional materials that are not feasible by conventional selective etching or delamination approaches.

METHODS

All chemicals were purchased from Sigma-Aldrich and used without further purifications. In a typical synthesis, a glass dish containing 50 mL of an aqueous solution of 20 mM SDS (dodecylsulfate, sodium salt), 25 mM zinc nitrate, and 25 mM hexamethylenetetramine was placed in a convection oven set at 90 °C for 4 h. After that, a continuous membrane formed on the water surface. This membrane was scooped by a silicon substrate or carbon film covered TEM copper grid for characterization. The morphology and structural characterizations of the NMs were performed with a LEO 1530 scanning electron microscope, a Philips CM200UT transmission electron microscope, and a Thermal Scientific K-Alpha small spot photoelectron spectrometer system. Small-angle XRD was taken by a Hi-Star 2D X-ray diffractometer, and powder diffraction was taken by a STOE powder diffractometer. The current−voltage characteristics of the single NM FETs were measured using a semiconductor parameter analyzer (Agilent 4155B) in the dark to avoid any light-induced photocurrents.

REFERENCES AND NOTES

1. Eda, G.; Fanchini, G.; Chhowalla, M. Large-Area Ultrathin Films of Reduced Graphene Oxide as a Transparent and Flexible Electronic Material. *Nat. Nanotechnol.* **2008**, *3*, 270–274.
2. Park, S. I.; Xiong, Y. J.; Kim, R. H.; Elvikis, P.; Meitl, M.; Kim, D. H.; Wu, J.; Yoon, J.; Yu, C. J.; Liu, Z. J.; Choquette, K.; Rogers, J. A.; *et al.* Printed Assemblies of Inorganic Light-Emitting Diodes for Deformable and Semitransparent Displays. *Science* **2009**, *325*, 977–981.
3. Monch, I.; Schumann, J.; Stockmann, M.; Arndt, K. F.; Schmidt, O. G. Multifunctional Nanomembranes Self-Assembled into Compact Rolled-Up Sensor-Actuator Devices. *Smart Mater. Struct.* **2011**, *20*, 085016.
4. Rao, C. N. R.; Sood, A. K.; Subrahmanyam, K. S.; Govindaraj, A. Graphene: The New Two-Dimensional Nanomaterial. *Angew. Chem., Int. Ed.* **2009**, *48*, 7752–7777.
5. Bonaccorso, F.; Sun, Z.; Hasan, T.; Ferrari, A. C. Graphene Photonics and Optoelectronics. *Nat. Photonics* **2010**, *4*, 611–622.
6. Rogers, J. A.; Lagally, M. G.; Nuzzo, R. G. Synthesis, Assembly and Applications of Semiconductor Nanomembranes. *Nature* **2011**, *477*, 45–53.
7. Huang, M. H.; Cavallo, F.; Liu, F.; Lagally, M. G. Nanomechanical Architecture of Semiconductor Nanomembranes. *Nanoscale* **2011**, *3*, 96–120.
8. Menard, E.; Lee, K. J.; Khang, D. Y.; Nuzzo, R. G.; Rogers, J. A. A Printable Form of Silicon for High Performance Thin Film Transistors on Plastic Substrates. *Appl. Phys. Lett.* **2004**, *84*, 5398–5400.
9. Verma, V. P.; Das, S.; Lahiri, I.; Choi, W. Large-Area Graphene on Polymer Film for Flexible and Transparent Anode in Field Emission Device. *Appl. Phys. Lett.* **2010**, *96*, 203108.
10. Sun, Y. G.; Rogers, J. A. Inorganic Semiconductors for Flexible Electronics. *Adv. Mater.* **2007**, *19*, 1897–1916.
11. Yuan, H. C.; Celler, G. K.; Ma, Z. Q. 7.8-GHz Flexible Thin-Film Transistors on a Low-Temperature Plastic Substrate. *J. Appl. Phys.* **2007**, *102*, 034501.
12. Yang, W. Q.; Yang, H. J.; Qin, G. X.; Ma, Z. Q.; Berggren, J.; Hammar, M.; Soref, R.; Zhou, W. D. Large-Area InP-Based Crystalline Nanomembrane Flexible Photodetectors. *Appl. Phys. Lett.* **2010**, *96*, 121107.
13. Sanchez-Perez, J. R.; Boztug, C.; Chen, F.; Sudradjat, F. F.; Paskiewicz, D. M.; Jacobson, R. B.; Lagally, M. G.; Paiella, R. Direct-Bandgap Light-Emitting Germanium in Tensilely Strained Nanomembranes. *Proc. Natl. Acad. Sci. U.S.A.* **2011**, *108*, 18893–18898.
14. Kim, R. H.; Kim, D. H.; Xiao, J. L.; Kim, B. H.; Park, S. I.; Panilaitis, B.; Ghaffari, R.; Yao, J. M.; Li, M.; Liu, Z. J.; *et al.* Waterproof AllnGaP Optoelectronics on Stretchable Substrates with Applications in Biomedicine and Robotics. *Nat. Mater.* **2010**, *9*, 929–937.
15. Viventi, J.; Kim, D. H.; Moss, J. D.; Kim, Y. S.; Blanco, J. A.; Annetta, N.; Hicks, A.; Xiao, J. L.; Huang, Y. G.; Callans, D. J.; *et al.* A Conformal, Bio-Interfaced Class of Silicon Electronics for Mapping Cardiac Electrophysiology. *Sci. Transl. Med.* **2010**, *2*, 24ra22.
16. Yuan, H. C.; Qin, G. X.; Celler, G. K.; Ma, Z. Q. Bendable High-Frequency Microwave Switches Formed with Single-Crystal

Silicon Nanomembranes on Plastic Substrates. *Appl. Phys. Lett.* **2009**, *95*, 043109.

17. Lee, K. J.; Meitl, M. A.; Ahn, J. H.; Rogers, J. A.; Nuzzo, R. G.; Kumar, V.; Adesida, I. Bendable GaN High Electron Mobility Transistors on Plastic Substrates. *J. Appl. Phys.* **2006**, *100*, 124507.

18. Ko, H. C.; Baca, A. J.; Rogers, J. A. Bulk Quantities of Single-Crystal Silicon Micro-/Nanoribbons Generated from Bulk Wafers. *Nano Lett.* **2006**, *6*, 2318–2324.

19. Kim, S.; Wu, J. A.; Carlson, A.; Jin, S. H.; Kovalsky, A.; Glass, P.; Liu, Z. J.; Ahmed, N.; Elgan, S. L.; Chen, W. Q.; *et al.* Microstructured Elastomeric Surfaces with Reversible Adhesion and Examples of Their Use in Deterministic Assembly by Transfer Printing. *Proc. Natl. Acad. Sci. U.S.A.* **2010**, *107*, 17095–17100.

20. Yoon, J.; Jo, S.; Chun, I. S.; Jung, I.; Kim, H. S.; Meitl, M.; Menard, E.; Li, X. L.; Coleman, J. J.; Paik, U.; *et al.* GaAs Photovoltaics and Optoelectronics Using Releasable Multilayer Epitaxial Assemblies. *Nature* **2010**, *465*, 329–U80.

21. Coleman, J. N.; Lotya, M.; O'Neill, A.; Bergin, S. D.; King, P. J.; Khan, U.; Young, K.; Gaucher, A.; De, S.; Smith, R. J.; *et al.* Two-Dimensional Nanosheets Produced by Liquid Exfoliation of Layered Materials. *Science* **2011**, *331*, 568–571.

22. Radisavljevic, B.; Radenovic, A.; Brivio, J.; Giacometti, V.; Kis, A. Single-Layer MoS(2) Transistors. *Nat. Nanotechnol.* **2011**, *6*, 147–150.

23. Schliehe, C.; Juarez, B. H.; Pelletier, M.; Jander, S.; Greshnykh, D.; Nagel, M.; Meyer, A.; Foerster, S.; Kornowski, A.; Klinke, C.; Weller, H. Ultrathin PbS Sheets by Two-Dimensional Oriented Attachment. *Science* **2010**, *329*, 550–553.

24. Yu, T.; Lim, B.; Xia, Y. N. Aqueous-Phase Synthesis of Single-Crystal Ceria Nanosheets. *Angew. Chem., Int. Ed.* **2010**, *49*, 4484–4487.

25. Yang, J. P.; Fendler, J. H. Morphology Control of PbS Nanocrystallites, Epitaxially under Mixed Monolayers. *J. Phys. Chem.* **1995**, *99*, 5505–5511.

26. Yang, J. P.; Meldrum, F. C.; Fendler, J. H. Epitaxial-Growth of Size-Quantized Cadmium-Sulfide Crystals under Arachidic Acid Monolayers. *J. Phys. Chem.* **1995**, *99*, 5500–5504.

27. Yi, K. C.; Horvolgyi, Z.; Fendler, J. H. Chemical Formation of Silver Particulate Films under Monolayers. *J. Phys. Chem.* **1994**, *98*, 3872–3881.

28. Vayssieres, L. Growth of Arrayed Nanorods and Nanowires of ZnO from Aqueous Solutions. *Adv. Mater.* **2003**, *15*, 464–466.

29. Ligier, V.; Wery, M.; Hihn, J. Y.; Faucheu, J.; Tachez, M. Formation of the Main Atmospheric Zinc End Products: $NaZn_4Cl(OH)_6SO_4 \cdot 6H_2O$, $Zn_4SO_4(OH)_6 \cdot nH_2O$ and $Zn_4Cl_2(OH)_4SO_4 \cdot 5H_2O$ in $[Cl^-]$ $[SO_4{}^{2-}]$ $[HCO_3{}^-]$ $[H_2O_2]$ Electrolytes. *Corros. Sci.* **1999**, *41*, 1139–1164.

30. Morin, S. A.; Forticaux, A.; Bierman, M. J.; Jin, S. Screw Dislocation-Driven Growth of Two-Dimensional Nanoplates. *Nano Lett.* **2011**, *11*, 4449–4455.

31. Zhang, W. X.; Yanagisawa, K. Hydrothermal Synthesis of Zinc Hydroxide Chloride Sheets and Their Conversion to ZnO. *Chem. Mater.* **2007**, *19*, 2329–2334.

32. Izaki, M.; Omi, T. Transparent Zinc Oxide Films Prepared by Electrochemical Reaction. *Appl. Phys. Lett.* **1996**, *68*, 2439–2440.

33. Sofos, M.; Goldberger, J.; Stone, D. A.; Allen, J. E.; Ma, Q.; Herman, D. J.; Tsai, W. W.; Lauhon, L. J.; Stupp, S. I. A Synergistic Assembly of Nanoscale Lamellar Photoconductor Hybrids. *Nat. Mater.* **2009**, *8*, 68–75.

34. Altuntasoglu, O.; Matsuda, Y.; Ida, S.; Matsumoto, Y. Syntheses of Zinc Oxide and Zinc Hydroxide Single Nanosheets. *Chem. Mater.* **2010**, *22*, 3158–3164.

35. Liang, C. H.; Shimizu, Y.; Masuda, M.; Sasaki, T.; Koshizaki, N. Preparation of Layered Zinc Hydroxide/Surfactant Nanocomposite by Pulsed-Laser Ablation in a Liquid Medium. *Chem. Mater.* **2004**, *16*, 963–965.

36. Evans, D. G.; Slade, R. C. T. Structural Aspects of Layered Double Hydroxides. *Struct. Bonding* **2006**, *119*, 1–87.

37. Li, P.; Wei, Y.; Liu, H.; Wang, X. K. Growth of Well-Defined ZnO Microparticles with Additives from Aqueous Solution. *J. Solid State Chem.* **2005**, *178*, 855–860.

38. Tan, Y. W.; Steinmiller, E. M. P.; Choi, K. S. Electrochemical Tailoring of Lamellar-Structured ZnO Films by Interfacial Surfactant Templating. *Langmuir* **2005**, *21*, 9618–9624.

39. Moretti, G. Auger Parameter and Wagner Plot in the Characterization of Chemical States By X-ray Photoelectron Spectroscopy: A Review. *J. Electron Spectrosc. Relat. Phenom.* **1998**, *95*, 95–144.

40. Vanenckevort, W. J. P.; Vanderlinden, W. H. Relation between Etch Pits or Growth Hillocks and Dislocations on the (111) Faces of Potassium Aluminum Alum. *J. Cryst. Growth* **1979**, *47*, 196–202.

41. Gutkin, M. Y.; Sheinerman, A. G. Split and Sealing of Dislocated Pipes at the Front of a Growing Crystal. *Phys. Status Solidi B* **2004**, *241*, 1810–1826.

42. Qian, W.; Rohrer, G. S.; Skowronski, M.; Doverspike, K.; Rowland, L. B.; Gaskill, D. K. Open-Core Screw Dislocations in Gan Epilayers Observed by Scanning Force Microscopy and High-Resolution Transmission Electron-Microscopy. *Appl. Phys. Lett.* **1995**, *67*, 2284–2286.

43. Heindl, J.; Strunk, H. P.; Heydemann, V. D.; Pensl, G. Micropipes: Hollow Tubes in Silicon Carbide. *Phys. Status Solidi A* **1997**, *162*, 251–262.